Different stages of chemical alteration on metabasaltic rocks in the subduction channel: Evidence from the Western Tianshan metamorphic belt, NW China

Yuanyuan Xiao [1, 2, 3, *], Yaoling Niu [1, 2, 4], Kuo-Lung Wang [3], Yoshiyuki Iizuka [3], Jinyan Lin [5], Dong Wang [1, 2], Yulong Tan [5], Guodong Wang [1,2]

[1] Institute of Oceanology, Chinese Academy of Sciences, Qingdao, 266071, China

[2] Laboratory for Marine Geology, Qingdao National Laboratory for Marine Science and Technology, Qingdao 266061, China

[3] Institute of Earth Sciences, Academia Sinica, Taipei, 11529, Taiwan

[4] Department of Earth Sciences, Durham University, Durham, DH1 3LE, UK

[5] Department of Geology, Northwest University, Xi'an, 710069, China

*Corresponding author: Dr Yuanyuan XIAO. Telephone: +86-0532-82898035. E-mail: yuanyuan_xiao@foxmail.com.

Abstract: To understand the geochemistry of subduction zone metamorphism, especially the large-scale mass transfer at forearc to subarc depths, we carried out a detailed study of a ~ 1.5 m size metabasaltic block with well-preserved pillow structures from the Chinese Western Tianshan high- to ultrahigh-pressure metamorphic belt. This metabasaltic block is characterized by omphacite-rich interiors gradually surrounded by abundant channelized (veins) glaucophane-rich patches toward the rims. The glaucophane-rich rims share the same peak metamorphic conditions with omphacite-rich interiors, but have experienced stronger blueschist-facies overprinting during exhumation. Representative samples from the glaucophane-rich rims and omphacite-rich interiors yield a well-defined Rb-Sr isochron age of 307±23 Ma, likely representing this overprinting event. Both glaucophane-rich rims and omphacite-rich interiors show elevated K-Rb-Cs-Ba-Pb-Sr contents relative to their protolith, reflecting a large-scale enrichment of these elements and formation of abundant phengite during subduction. Compared with the omphacite-rich interiors, the glaucophane-rich rims have gained rare earth elements (REEs, > 25%), U-Th (~ 75%), Pb-Sr (> 100%) and some transition metals like Co and Ni (25 – 50%), but lost P (~ 75%), Na (> 25%), Li and Be (~ 50%); K-Rb-Cs-Ba show only 10% loss. These chemical changes would be caused by serpentinite-derived fluids during the exhumation in the subduction channel. Therefore, there are two stages of fluid action in the subduction channel. As the formation of phengite stabilizes K-Rb-Cs-Ba at the first stage, the residual fluids released from the phengite-rich metabasaltic rocks would be depleted in these elements, which are unlikely to contribute to elevated contents of these elements in arc magmas if phengite remains stable at subarc depths. In addition, the decrease of U/Pb ratios as the preferred enrichment of Pb over U in the eclogitic rocks during the first stage chemical alteration may further lead to the lower radiogenic Pb isotope component of the deeply subducted ocean crust with time, which is inconsistent with the high radiogenic Pb isotope component of high μ (= $^{238}U/^{204}Pb$) basalts.

Keywords: subduction ; channelized glaucophane-rich rims surrounding omphacite-rich interiors; mass transfer; subduction zone magmatism; mantle heterogeneity

1 Introduction

The subduction zone metamorphism and related geochemical processes are significant for arc magmatism and mantle heterogeneity, which have attracted much attention in recent years (e.g., Kerrick and Connolly, 2001; Kelley et al., 2005; Keppler, 1996; McCulloch and Gamble, 1991; Niu et al., 2002; Niu and O'Hara, 2003; Niu, 2009; Tatsumi, 2005; John et al., 2012; Bebout, 2014; Marschall and Schumacher, 2012; Spandler and Pirard, 2013; Zheng and Chen, 2016). These studies have found that the geochemical behaviors of chemical elements during subduction zone metamorphism are much more complex than previously inferred through subduction zone magmatism, and they are not only controlled by the presence and stability of variable minerals (e.g., El Korh et al., 2009; Hermann and Rubatto, 2009; Spandler et al., 2003; Xiao et al., 2012, 2013, 2014, 2016) but also affected by the thermal structure of subduction zones (van Keken et al., 2011; Zheng et al., 2016) and the physicochemical properties of fluids, e.g., fluids with dissolved Na-Al silicates or halogen, supercritical fluids (Gao et al., 2007; Gao and Klemd, 2001; Haase et al., 2015; Hermann et al., 2006; John et al., 2008, 2012; Rubatto and Hermann, 2003; Schmidt et al., 2004; Spandler and Hermann, 2006; Zack and John, 2007; Zheng et al., 2011). The complex subduction-exhumation processes (i.e., multiple subduction-exhumation cycles) in subduction channels proposed in recent studies may lead to more complicated geochemical processes and consequences (Rubatto et al., 2011; Zheng and Hermann, 2014; Li et al., 2016; Xiao et al., 2016). Hence, the information on large-scale fluid-rock interactions in subduction

channels is critically needed for understanding of large-scale mass transfer from the subducting slab to the overlying mantle wedge, which is essential towards a genuine understanding of arc magmatism and mantle heterogeneity.

It has been proposed that large-scale fluid fluxes and channelized fluids can facilitate element mobility in subduction zones (e.g., Ague, 2011; Bebout, 2007; Herms et al., 2012; John et al., 2008; Spandler and Hermann, 2006; Zack and John, 2007; Li et al., 2013; Bebout and Penniston-Dorland, 2016). In order to better understand the large-scale mass transfer from the subducting slab to the overlying mantle wedge, it is best to study subduction-zone metamorphic rocks affected by large-scale fluid flows, the conduit of which is manifested by large-scale veins (e.g., John et al., 2012; Spandler and Hermann, 2006; van der Straaten et al., 2008, 2012). This study focuses on a ~ 1.5 m size metabasaltic block with well-preserved pillow structures from the Chinese Western Tianshan high-pressure (HP) to ultrahigh pressure (UHP) metamorphic belt (Figs. 1 and 2). Through a combined study of mineralogy, petrology and geochemistry, we discuss the behaviors of chemical elements in response to different stages of large-scale fluid-rock interactions, which offer insights into the possible large-scale mass transfer, contributing to our understanding of subduction zone magmatism and mantle heterogeneity.

2 Field Geology and Petrography

The Western Tianshan HP-UHP metamorphic belt in NW China (Fig. 1) represents

a paleo-convergent plate margin associated with successive northward subduction of the South Tianshan ocean crust beneath the Tarim Block during the Carboniferous (Gao and Klemd, 2003; Gao et al., 1999; Su et al., 2010; Klemd et al., 2011; Yang et al., 2013). This HP-UHP metamorphic belt is composed of pelitic schist, marble, serpentinite, blueschist and eclogite (Gao and Klemd, 2001; Wei et al., 2009; Li et al., 2012; Lü et al., 2013; Shen et al., 2015; Klemd et al., 2011; Yang et al., 2013) with protoliths of sandstone, pelite, carbonates, peridotite and basalts respectively (Ai et al., 2006; Gao and Klemd, 2003; Xiao et al., 2012). The Sm-Nd isochron age of ~ 343 Ma indicates the time of subduction metamorphism (Gao and Klemd, 2003), whereas the $^{40}Ar/^{39}Ar$ and Rb–Sr ages of ~ 310 Ma for white mica are thought to represent the time of retrograde overprint during exhumation (Klemd, 2005). Based on recent findings of coesite and their distributions (e.g., Lü et al., 2008, 2009, 2013, 2014; Lü and Zhang, 2012), the Chinese Western Tianshan metamorphic belt has been classified into HP and UHP metamorphic sub-units (Fig. 1; Lü and Zhang, 2012).

Numerous studies have shown large-scale fluid-rock interactions in the Chinese Western Tianshan HP-UHP metamorphic belt (Gao and Klemd, 2001; Gao et al., 2007; John et al., 2008, 2012; van der Straaten et al., 2008, 2012; Beinlich et al., 2010; Lü et al., 2012; Li et al., 2013, 2016). Our sampling location is along the Atantayi River (Fig. 1). The studied metabasaltic block with well-preserved pillow structures (Fig. 2) is a boulder, which has recently rolled from the steep mountain slope, and has omphacite-rich domains in the interiors, gradationally surrounded by abundant

106 channelized glaucophane-rich patches toward the rims (Figs. 2a-c and 3a). Both
107 omphacite-rich interiors and channelized glaucophane-rich rims are characteristically
108 dominated by omphacite, glaucophane, phengite, and epidote as well as locally
109 accumulated garnet plus some quartz, apatite, and carbonates, but glaucophane and
110 epidote modes increase with decreasing omphacite mode toward rims (e.g., Fig. 2d-g).

111 Samples for this study are taken as a drilling core from this metabasaltic block with
112 well-preserved pillow structures, ~10 cm long with a diameter of 2.5 cm (Fig. 2). The
113 drilling core is divided into 4 sections for convenience, labelled as 22A, 22B, 22C and
114 22D from the rim surface to the interior (Fig. 2c). These four rock samples contain
115 similar mineral assemblages with varying modal abundances. Samples 22C and 22D
116 represent the omphacite-rich domain dominated by omphacite and phengite (Fig. 2d,e),
117 while 22A and 22B represent the glaucophane-rich rim with abundant glaucophane and
118 epidote (Fig. 2f,g). No garnet is present in these samples.

119 Samples 22C and 22D are mainly composed of omphacite and phengite matrix
120 with some epidote and glaucophane porphyroblasts (Fig. 3c-f). Carbonate is locally
121 present together with coarse-grained omphacite, phengite, and apatite (Fig. 3d,e).
122 Epidote and glaucophane porphyroblasts are always euhedral and contain abundant
123 inclusions of omphacite, phengite, carbonate, rutile and titanite (Fig. 4a,b).
124 Glaucophane porphyroblasts also contain epidote inclusions. Rutile occurs as
125 inclusions (Fig. 4a) and is locally replaced by titanite (Fig. 4b,c). Titanite is commonly
126 present as poikiloblasts containing omphacite, phengite and quartz inclusions (Fig. 4c).

Samples 22A and 22B mainly comprise coarse-grained epidote and glaucophane (Fig. 3b) with phengite and much decreased omphacite (Fig. 4f). Carbonate, apatite and titanite are randomly present (Fig. 4f). More epidote and glaucophane with titanite occur as poikiloblasts and contain omphacite, phengite and carbonate (Fig. 4d-f), reflecting stronger blueschist-facies overprinting. Allanite is also present in epidote porphyroblast (Fig. 4e). Rutile has been entirely replaced by titanite.

3 Analytical Methods

Each rock sample (22A, 22B, 22C and 22D) from the top surface to the bottom of the drilling core from the metabasaltic block (Fig. 2c) has been further cut into three pieces, i.e., the middle chip of the section was mounted in epoxy resin and polished for mineral analysis (Fig. 2d-g), while the other two chips were ultrasonically cleaned before hand-crushed in an agate mortar into powders for bulk-rock analysis. Considering the highly heterogeneous mineral distribution in metamorphic rocks, especially the along-core modal variation, this division method can make the bulk-rock composition of sample powders to be representative and consistent with the mineral assemblages as observed in thin sections. Thin sections for the other two drilling cores from the same metabasaltic block have also been prepared for petrography study (e.g., Fig. 3).

3.1 Mineral compositions

Major elements of hydrous minerals were analyzed using a JXA-8100 electron

147 probe micro-analyzer (EPMA) at Chang'an University, China. The analyses were
148 performed using 15 kV accelerating voltage and 10 nA probe current. Standards used
149 for calibration are: albite for Na, quartz for Si, orthoclase for K, apatite for P and Ca,
150 magnetite for Fe, pyrophanite for Mn and Ti, chromite for Cr and Fe, forsterite for Mg,
151 and jadeite for Al (Xiao et al., 2013). Representative analytical results of mineral
152 major element contents using EPMA are given in Table S.1. Mineral trace elements
153 and major elements for anhydrous minerals were measured on polished sections by
154 using an LA-ICP-MS (Agilent 7500a with GeoLas 2005 193 Eximer Laser sampler)
155 at the State Key laboratory of Continental Dynamics, Northwest University, China. The
156 repetition rate of laser ablation is 6 Hz, and the pit size is 32 μm. During each analysis,
157 the acquisition times for the background (gas blank) and the sample ablation are 20 –
158 30 s and 50 s respectively. United States Geological Survey (USGS) glasses BCR-2G,
159 BHVO-2G, BIR-1G and one synthetic glass GSE-1G (Guillong et al., 2005; Jochum
160 et al., 2005) are used as reference materials. For anhydrous minerals (i.e., omphacite,
161 and titanite), instead of using the internal standard for calibration, the concentrations
162 of all the elements of interest (both major and trace elements) are analyzed
163 simultaneously and calibrated through an internal standard-independent calibration
164 method (see Liu et al., 2008). For hydrous minerals, major elements analyzed by using
165 EPMA are chosen as internal standards for calibration, i.e., Si for amphibole, epidote
166 group minerals and phengite; Ca for apatite and carbonate. The analytical uncertainty
167 is within 10% and the precision determined by repeated analysis of GSE-1G is

generally better than 5%. During analysis, inclusions are purposely avoided. Analytical results of mineral trace element contents are given in Table S.2.

3.2 Bulk-rock major and trace elements

Bulk-rock major and trace element contents were analyzed at Northwest University, China. The major elements were analyzed by using X-ray fluorescence (Rigaku RIX 2100 XRF) on fused glass disks with analytical precision better than 5% as determined by duplicate analyses. An additional sample powder ~ 1g is heated in a muffle furnace at 1000 °C for loss on ignition (LOI) determination.

For the trace element analysis, 50 mg sample powders were digested in an HF+HNO_3 mix in high-pressure Teflon bombs at 190 °C for 48 h. After being dried, 3 ml 50% HNO_3 was added and sample powders was dissolved again in high-pressure Teflon bombs at 150 °C for 12 h. Rh as an internal standard was added to sample solutions, which are finally diluted to 80 g. ICP-MS (Agilent 7500a) was used for trace element analysis with analytical accuracy better than 5% for most trace elements. The analytical results of bulk-rock compositions are given in Table 1.

3.3 Sr-Nd isotope

Sample digestion for Sr-Nd isotope analysis was done at the National Cheng-Kung University, Taiwan. Sample powder of 100 mg was decomposed in a high-pressure bomb by 3 ml concentrated HF–HNO_3 mixture at 190 °C for 24 h. After being dried, 5 ml 6N HCl was added, followed by conversion to nitrate form (see Liu

et al., 2015). The Sr and Nd separation was done at the Institute of Earth Sciences, Academia Sinica in Taipei through a two-column technique using Bio-Rad AG50W-X8 and Ln-B25-A (Eichron) resins respectively (Jahn et al., 2009).

Finnigan MAT-262 thermal ionization mass spectrometer (TIMS) and Finnigan Triton TIMS were used for Sr and Nd isotope analyses respectively. The Sr and Nd isotopic ratios were normalized against the value of $^{86}Sr/^{88}Sr=0.1194$ and $^{146}Nd/^{144}Nd=0.7219$ respectively. The 2σ values for all the analyses are less than 0.000007 for $^{87}Sr/^{86}Sr$ and less than 0.000008 for $^{143}Nd/^{144}Nd$ (Table S.3). The measured isotopic ratio for NBS987-Sr standard is $^{87}Sr/^{86}Sr=0.710245\pm0.000010$ (2σ) and that for JMC Nd standard is $^{143}Nd/^{144}Nd=0.511817\pm0.0000007$ (2σ), which are consistent with the data of Shellnutt et al. (2012; 0.710248±0.00001, 2σ) and Jahn et al. (2009; 0.511821±0.000016, 2σ) respectively.

4 Analytical results

4.1 Mineral compositions

In chondrite normalized trace element diagram (Fig. 5), epidote from 22A (representing the glaucophane-rich rim) show greater variations of Th, U and rare earth elements (REEs) than 22D (representing the omphacite-rich domain; $10 – 10^4$ times vs. $10^2 – 10^3$ times the chondritic values, Fig. 5a). Allanite as the core of an epidote crystal from 22A contains the highest REEs (e.g., 3192 ppm in analyzed point 22A-C4-1, Table S.2; Figs. 4e and 5a), while some other epidote crystals from 22A show only

several ppm REEs (Table S.2). Apatite also shows consistently high REEs-Th-U-Sr (up to 10 – 100 times the chondritic values, Fig. 5c). Carbonate has high Sr contents (> 10 times the chondritic value, Fig. 5e). All the analyzed points on phengite from both 22D and 22A generally share a similarly high contents of large ion lithophile element (LILE), including Ba-Rb-Cs (10 – 10^3 times the chondritic values, Fig. 5b). Glaucophane shows low contents for most trace elements of interest (Fig. 5f) except Li and Be (up to > 10 ppm Li and several ppm Be; Table S.2). Glaucophane from 22D shows generally higher Be than that from 22A (several ppm vs. lower than detection limits; Table S.2).

Titanite is characterized by high Nb and Ta contents (up to 3 orders of magnitude higher than the chondritic values) and heavy rare earth elements (HREEs; ~ 10 times the chondritic values, Fig. 5d). Omphacite also shows low contents for most trace elements of interest (Fig. 5f), but contains the highest Li and Be among all the analyzed minerals (tens of ppm Li and several ppm Be; Table S.2).

4.2 Bulk-rock major and trace element contents

From 22D to 22A with increasing extents of blueschist-facies overprinting, major element contents vary, reflecting controls of mineral modal abundances. Al_2O_3 content obviously increases towards glaucophane-rich rims (Table 1), consistent with the increasing modal abundance of epidote resulting from addition of Al associated with blueschist-facies overprinting. Whereas, Na_2O and P_2O_5 contents slightly decrease towards glaucophane-rich rims (Table 1; Fig. 6b), consistent with less omphacite and apatite respectively.

By using commonly accepted immobile high field strength elements (HFSEs) and HREEs (Pearce, 2008), the four rock samples in this study plot within the mid-ocean ridge basalts (MORB)-oceanic island basalts (OIB) array, close to the data point for enriched-MORB (E-MORB) and OIB (Fig. 6a). Furthermore, these rocks consistently show similar trace element patterns to that of E-MORB (Fig. 6b) except for the notably higher K-Rb-Ba-Pb-Sr contents and stronger L(light-)REE/HREE fractionation. With increasing extents of blueschist-facies overprinting from 22D to 22A, contents of Th-U-REEs-Pb-Sr and some siderophile elements (e.g., Co, Ni) variably increase (Fig. 6b; Table 1), while Li and Be contents tend to decrease (Table 1). K-Rb-Cs-Ba contents show only slight differences, and no obvious change of HFSEs or Sc-V among the four rocks (Fig. 6b; Table 1).

4.3 Sr-Nd isotopes

The four bulk samples yield a well-defined Rb-Sr isochron age of 307±23 Ma (MSWD=6.9) and an initial $^{87}Sr/^{86}Sr$ ratio of 0.70461±0.00015 (Fig. 7a; using ISOPLOT 3 of Ludwig, 2003). This Rb-Sr isochron age, within error, overlaps with the age of the rehydration overprint at ~ 310 Ma for the Chinese Western Tianshan HP-UHP metamorphic belt in literature (Gao and Klemd, 2003; Klemd, 2005; Klemd et al., 2011), and thus represents the time of blueschist-facies overprinting during exhumation. The limited range of $^{147}Sm/^{144}Nd$ ratios (0.143 – 0.148) does not give a useful Sm-Nd isochron age. The initial Sr-Nd isotope values of the four samples calculated at 310 Ma give $(^{87}Sr/^{86}Sr)_{310Ma}$ of 0.704560 to 0.704614 and $\varepsilon_{Nd}(t)$ values of

+1.9 to +2.1 at t = 310 Ma (Table S.3). In Fig. 7b, all the Sr-Nd isotope data points for the four samples plot as a cluster in the MORB-OIB mantle array.

5 Discussion

5.1 Geochemical behaviors of chemical elements

The exhumed HP-UHP metamorphic rocks of oceanic subduction zones are always an integrated product, which is likely to have experienced a series of geochemical processes including seafloor alteration during protolith generation, chemical alteration during subduction and retrograde overprint during exhumation in the subduction channel (e.g., Xiao et al., 2016). As discussed above, mineral assemblages and mineral inclusions in glaucophane and epidote porphyroblasts from the glaucophane-rich rims and omphacite-rich interiors are similar (Figs. 2-4). This reflects that both glaucophane-rich rims and omphacite-rich interiors have experienced a similar eclogite-facies peak metamorphic condition. However, more epidote and glaucophane porphyroblasts replacing omphacite towards glaucophane-rich rims (Figs. 2 and 3) reflect that the glaucophane-rich rim experienced a greater extent of overprinting than the omphacite-rich interior. These petrological results indicate that our studied four rock samples have similarly experienced two main stages of geochemical alteration in the subduction channel with different extents of blueschist-facies overprinting. Therefore, it is important to identify various effects of these geochemical processes on the behaviors of chemical elements at different

stages.

5.1.1 Seafloor alteration

Ba and Rb have been found to behave similarly during subduction zone metamorphism as they are preferentially sequestered into phengite (e.g., Hermann and Rubatto, 2009; Xiao et al., 2012, 2014, 2016). However, it has been reported that seafloor alteration can lead to obvious enrichment of Rb (9 times of the original) but not Ba (Kelley et al., 2003). Hence, the rocks that have experienced seafloor alterations are expected to have low Ba/Rb ratios. In Fig. 8, the four rock samples show relatively lower Ba/Rb ratios than those of seafloor basalts while no fractionation of Ba/Rb ratios among these rock samples, probably indicating the effects of seafloor alteration on the trace element systematics of these rock samples.

5.1.2 The first stage chemical alteration during subduction

Given the E-MORB-like protolith composition as shown in Fig. 6, our rock samples show commonly elevated contents of K-Rb-Cs-Ba-Pb-Sr compared to those in E-MORB (Fig. 6b), and thus these elements cannot be inherited from the protolith. As all these four rock samples have experienced eclogite-facies metamorphism with different extents of blueschist-facies overprinting as manifested by mineral assemblages (Figs. 2 and 3), the consistency in the elevated contents of K-Rb-Cs-Ba-Pb-Sr in these rocks relative to their E-MORB-like protolith suggests that the large-scale enrichment of these elements occurred during the eclogite-facies

metamorphism when the first stage chemical alteration took place in the subduction channel before the blueschist-facies overprinting.

5.1.3 The second stage chemical alteration during exhumation

The blueschist-facies overprinting of metabasaltic pillow interiors and rims to variable extents represents the second stage chemical alteration in the subduction channel. We take omphacite-rich 22D with the least blueschist-facies overprint as representing the rock composition before this overprint. Considering the increasing extents of blueschist-facies overprinting from 22D to 22A (Figs. 2d-g and 3), the systematic elemental changes from 22D to 22A (Fig. 6b; Table 1) indicate that P-Na-Mg-K-Ca-Al-Fe, Th-U-REEs-Pb-Sr-Li-Be, some transition metals (e.g., Co and Ni) have been mobilized to varying extents, while Rb-Cs-Ba, HFSEs and Sc-V have been largely conserved with blueschist-facies overprinting at the second stage chemical alteration in the subduction channel.

To further understand the mass change with blueschist-facies overprinting during exhumation, we chose the highly overprinted glaucophane-rich 22A to compare with 22D in an isocon diagram (Fig. 9a). The slope of isocons defined by immobile SiO_2-MnO-TiO_2-Ta-Zr-Hf is 1.0073, very close to 1, and thus indicates a very small mass loss or gain (Grant, 2005). As the data points plotted above and below the isocon reflect the element gain and loss respectively, the most evident changes with blueschist-facies overprint are: (1) > 100 % Pb and Sr gain; (2) ~ 75 % U-Th gain; (3) > 25 % REEs gain; (4) 25 – 50 % transition metal (e.g., Ni and Co) gain; (5) ~ 25 % and

311 75 % Na and P loss respectively; (6) ~ 50 % Li and Be loss. On the other hand, Sc-V-Nb
312 and LILE (K-Rb-Cs-Ba) show insignificant changes from 22D to 22A, i.e., no more
313 than 10% gain or loss. Given the immobility of Ta, Zr and Hf, the increase of La/Ta and
314 Th/Nb ratios but the decrease of Ta/U and Nb/U ratios from 22D to 22A (Fig. 9b)
315 further reflects the addition of REEs (represented by La)-Th-U with blueschist-facies
316 overprinting.

317 **5.2 Controls on the geochemical behaviors of chemical elements**

318 Based on our previous studies (Xiao et al., 2014, 2016), the geochemical behaviors
319 of trace elements during subduction zone metamorphism have been found to be
320 controlled by a number of factors, particularly the formation and stability of specific
321 minerals in metamorphic rocks. Heterogeneous compositions of metamorphic minerals
322 and bulk rocks are determined by element availability, i.e., the inherited composition
323 and the competition between coexisting minerals (Xiao et al., 2016), which is also
324 controlled by the presence and stability of metamorphic minerals. For an open system,
325 variable physicochemical compositions and abundances of fluids can affect the
326 behaviors of chemical elements (e.g., John et al., 2012; Spandler and Hermann, 2006;
327 van der Straaten et al., 2008, 2012; Zack, 2007), and thus can further affect the
328 compositions of metamorphic minerals and bulk rocks. The studied metabasaltic block
329 has large-scale channelized (veins) glaucophane-rich rims surrounding the
330 omphacite-rich interiors. As veins represent previous fluid flow passages, the
331 large-scale channelized glaucophane-rich patches reflect the presence and action of

large-scale fluid flux in the subduction channel (Bebout, 2007).

As K-Rb-Cs-Ba-Pb-Sr are expected to be enriched in meta-sedimentary rocks (e.g., Breeding et al., 2004; Hermann and Spandler, 2008), the common enrichments of these elements during the first stage chemical alteration in the subduction channel may have resulted from addition of these elements by fluids released from subducting sediments. Furthermore, considering the significance of phengite in hosting K-Rb-Cs-Ba (Fig. 5b; e.g., Sorensen et al., 1997; Spandler et al., 2003; El Korh et al., 2009; Zheng et al., 2011; Xiao et al., 2014, 2016), this enrichment facilitates abundant phengite formation as observed (Fig. 3), which results in the great conservation of these elements during this process as manifested by even much higher contents of these elements in the four studied rock samples than those in OIB (Fig. 6b).

With the blueschist-facies overprinting during the second stage chemical alteration in the subduction channel, the increase of REEs-Sr-Pb-Th-U with increasing extents of blueschist-facies overprinting (Fig. 9) manifests precipitation of these elements in the form of epidote from external fluids (Figs. 5a and 10; e.g., Xiao et al., 2014, 2016). The obvious decrease of Li and Be contents during this process is consistent with the loss of Li and Be associated with the replacement of omphacite by glaucophane. Because transition metals are enriched in mantle rocks relative to mantle-derived basaltic rocks and show immobility during serpentinization (e.g., ~ 100 ppm vs. ~ 30 – ~ 50 ppm for Co, ~ 800 – ~ 2000 ppm vs. 10s – 100s ppm for Ni, Niu, 2004; Niu and Batiza, 1997), the correlated increase of Co and Ni contents from the omphacite-rich interior to the

353 glaucophane-rich rim (Fig. 8b) suggests that the fluids responsible for the
354 blueschist-facies overprinting may be derived from serpentinite (van der Straaten et al.,
355 2008, 2012), which is the most significant fluid budget in the subducting slab and
356 crucial for element mobility in the subduction channel (Barnes et al., 2014; Deschamps
357 et al., 2012; Herms et al., 2012; Rüpke, 2002, 2004; Scambelluri et al., 2014; Shen et al.,
358 2015; Spandler et al., 2014; Stern et al., 2006).

359 Whereas, K-Rb-Cs-Ba contents show rather insignificant changes (only ~ 10 %
360 loss) with blueschist-facies overprinting, although these elements were thought to be
361 easily mobilized with fluids, especially in an open system (e.g., Breeding et al., 2004;
362 van der Straaten et al., 2012; Xiao et al., 2014). This is different from the result of
363 recent studies by van der Straaten et al. (2008, 2012) for metabasaltic rocks with pillow
364 structures affected by similar blueschist-facies overprinting from the Chinese Western
365 Tianshan HP-UHP metamorphic belt, i.e., even up to ~ 200 % of K-Rb-Cs-Ba have
366 been gained during blueschist-facies overprinting. The insignificant mobility of LILEs
367 during blueschist-facies overprinting in our studied rocks may be attributed to the
368 significant conservation of LILEs in abundant phengite, the formation of which
369 resulted from the commonly great enrichments of LILEs during the first stage chemical
370 alteration in the subduction channel. Meanwhile, it also reflects insignificant addition
371 of LILEs by serpentinite-derived fluids during the blueschist-facies overprinting, which
372 thus cannot lead to the formation of more phengite. Hence, after the reaction between
373 phengite-rich metabasaltic rocks and large fluid fluxes derived from serpentinite,

K-Rb-Cs-Ba can be still largely conserved and show limited mobility. However, in studies of van der Straaten et al. (2008, 2012), phengite modal abundance in the eclogitic interior is much lower (e.g., no more than ~ 10 %, van der Straaten et al., 2008) while more phengite formed during blueschist-facies overprinting (e.g. ~ 20 %, van der Straaten et al., 2008) due to addition of the fluids from serpentinite but with crucial addition of sediment-derived component.

5.3 Geodynamic implications

The slab-mantle interface composed of diverse lithologies and characterized by high permeability can facilitate the formation of channelized fluids as well as intense fluid-rock interactions, which may enhance element mobility (e.g. Bebout, 2007; Beinlich et al., 2010; Breeding et al., 2004; John et al., 2008; Li et al., 2013; van der Straaten et al., 2008; Zheng, 2012). The common enrichment of K-Rb-Cs-Ba in our studied rocks during the first stage chemical alteration in the subduction channel reflects the mobility and introduction of these elements, most likely derived from dehydration of the subducting sediments. This enrichment facilitates abundant phengite formation as widely observed in our samples, while the residual fluids released from these phengite-rich metabasalts may be depleted in K-Rb-Cs-Ba. Furthermore, the conservation by the already present phengite and the low contents of K-Rb-Cs-Ba in the serpentinite-derived fluids during the second stage chemical alteration in the subduction channel result in no obvious change of these elements with the infiltration of large fluid fluxes (Fig. 2a). This indicates that the reaction between phengite-rich

metabasaltic rocks and large fluid fluxes mainly derived from dehydration of the serpentinites cannot make phengite breakdown/dissolved or lead K-Rb-Cs-Ba to be mobilized at forearc depths. Therefore, the elevated contents of K-Rb-Cs-Ba widespread in arc magmas (known as the arc signature, e.g., McCulloch and Gamble, 1991) may be caused by the phengite breakdown at subarc depths, where fluid mobile elements can be transferred from the subducting crust to the mantle (Zheng et al., 2016). Otherwise, it requires the involvement of supercritical fluids or hydrous melts originated from the subducting slab (e.g., Xiao et al., 2012, 2014).

On the other hand, with varying extents of element changes, element ratios (e.g., Nb/U, Ta/U, Ce/Pb, U/Pb) will change accordingly, including radioactive parent to radiogenic daughter element ratios (Fig. 9b). The common enrichment of Pb but insignificant alteration of U during the first stage chemical alteration in the subduction channel (Fig. 6b) indicates the decrease of U/Pb ratios in the highly eclogitized rocks (e.g., sample 22D), which will further result in the lower radiogenic Pb isotope component of the deep mantle with time after the continuous subduction of these materials. Hence, the high μ (HIMU; $\mu = {}^{238}U/{}^{204}Pb$) OIB may not be caused by the long time-integrated subducting MORB (e.g., Hofmann, 1997) but by the other mechanism. For example, Castillo (2015) has proposed that subducting ancient marine carbonates can lead to high μ component as high U but low Pb precipitated from seawater (Xiao et al., 2017).

6 Conclusions

In this study, the glaucophane-rich rims share the similar peak metamorphic conditions with omphacite-rich cores, but show stronger blueschist-facies overprinting during exhumation, the age of which has been constrained to be 307 ± 23 Ma (MSWD = 6.9) by a well-defined Rb-Sr isochron age. Our rock samples record at least two stages of chemical alteration in the subduction channel. During the first stage chemical alteration, K-Rb-Cs-Ba-Pb-Sr are pervasively enriched in the studied rocks, producing abundant phengite during subduction. The second stage chemical alteration with blueschist-facies overprinting resulted in the enrichment of REEs (> 25%), U-Th (> 50%), Pb-Sr (> 100%) added by fluids and depletion of P (~ 75%) - Li and Be (~ 50%) as the result of the formation of epidote and glaucophane at the expense of apatite and omphacite. The rather insignificant loss of K-Rb-Cs-Ba (< 10%) with blueschist-facies overprinting results from the conservation of these elements by already formed abundant phengite, indicating that the reaction of large fluid fluxes with phengite-rich metabasaltic rocks has limited effects on the mobility of K-Rb-Cs-Ba during exhumation. The phengite breakdown at subarc depths is the key to the elevated contents of these elements in arc magmas; otherwise, the other mechanisms like supercritical fluids or hydrous melts from subducting sediments may be responsible for the elevated K-Rb-Cs-Ba contents in arc magmas. As the decrease of U/Pb ratios in the highly eclogitized rocks results from the common enrichment of Pb but insignificant alteration of U during the first stage chemical alteration in the subduction

channel, it will further lead to the lower radiogenic Pb isotope component of the deeply subducted ocean crust with time, inconsistent with the feature of HIMU. Hence, the HIMU of OIB may be caused by the other mechanism, e.g., the subducting marine carbonates rather than the long time-integrated subducting MORB in the traditional model.

Acknowledgement

This study was supported by the National Natural Science Foundation of China (Grant numbers: 41572047 to Yuanyuan Xiao; 41630968 to Yaoling Niu), Laboratory for Marine Geology, Qingdao National Laboratory for Marine Science and Technology, China, the Excellent Young Project of Institute of Oceanology, Chinese Academy of Sciences (Y52221101Q) and the Special Research Program of the State Oceanic Administration of China (GASI-GEOGE-02) to Yuanyuan Xiao. We thank all the research staff in the Institute of Earth Sciences, Academia Sinica, Taiwan, especially people from the well-communicated geochemical group for their great supports. We also thank Dr. Yung-Hsin Liu, Mr. Yu-Shiang Wang and Ms Hui-Ho Hseih from Academia Sinica and Dr. Honglin Yuan, Dr. Xiaoming Liu, Mr. Jianqi Wang, Ms. Ye Liu, Dr. Chunrong Diwu, Dr. Hong Zhang, Dr. Mengning Dai and Ms. Chunlei Zong from Northwest University, China for their great helps for geochemical analytical works. Prof. Y.-F. Zheng and two anonymous reviewers are greatly appreciated for their constructive comments that greatly help improvement of this manuscript.

References

Ague, J.J., 2011. Extreme channelization of fluid and the problem of element mobility during Barrovian metamorphism. American Mineralogist 96(2-3), 333-352.

Ai, Y.L., Zhang, L.F., Li, X.P., Qu, J.F., 2006. Geochemical characteristics and tectonic implications of HP-UHP eclogites and blueschists in Southwestern Tianshan, China. Progress in Natural Science 16(6), 624 - 632.

Barnes, J.D. et al., 2014. Geochemistry of Alpine serpentinites from rifting to subduction: A view across paleogeographic domains and metamorphic grade. Chemical Geology 389, 29-47.

Bebout, G.E., 2007. Metamorphic chemical geodynamics of subdution zones. Earth and Planetary Science Letters 260, 373-393.

Bebout, G.E., 2014. 4.20 - Chemical and Isotopic Cycling in Subduction Zones. In: Turekian, H.D.H.K. (Ed.), Treatise on Geochemistry (Second Edition). Elsevier, Oxford, pp. 703-747.

Bebout, G.E., Penniston-Dorland, S.C., 2016. Fluid and mass transfer at subduction interfaces—The field metamorphic record. Lithos 240–243, 228-258.

Beinlich, A., Klemd, R., John, T., Gao, J., 2010. Trace-element mobilization during Ca-metasomatism along a major fluid conduit: Eclogitization of blueschist as a consequence of fluid–rock interaction. Gechimica et Cosmochimica Acta 74(6), 1892-1922.

Breeding, C.M., Ague, J.J., Bröcker, M., 2004. Fluid-metasedimentary rock interactions in subduction-zone mélange: Implicaitions for the chemical composition of arc magmas. Geology 32, 1041-1044.

Castillo, P.R., 2015. The recycling of marine carbonates and sources of HIMU and FOZO ocean island basalts. Lithos 216, 254-263.

Deschamps, F. et al., 2012. Behavior of fluid-mobile elements in serpentines from abyssal to subduction environments: Examples from Cuba and Dominican Republic. Chemical Geology 312–313, 93-117.

El Korh, A., Schmidt, S.T., Ulianov, A., Potel, S., 2009. Trace element partitioning in HP-LT metamorphic assemblages during subduction-related metamorphism, Ile de Groix, France: a detailed LA-ICPMS Study. Journal of Petrology 50, 1107-1148.

El Korh, A., Schmidt, S.T., Ulianov, A., 2009. Effects of retrogression on trace element contents of metabasites, Ile de Groix, France, Goldschmidt Conference Abstract, Davos, Switzerland, pp. A325.

Gao, J., John, T., Klemd, R., Xiong, X.M., 2007. Mobilization of Ti-Nb-Ta during subduction: Evidence from rutile-bearing dehydration segregations and veins hosted in eclogite, Tianshan, NW China. Geochimica et Cosmochimica Acta 71, 4974-4996.

Gao, J., Klemd, R., 2001. Primary fluids entrapped at blueschist to eclogite transition: evidence from the Tianshan meta-subduction complex in northwestern China. Contributions to Mineralogy and Petrology 142, 1-14.

Gao, J., Klemd, R., 2003. Formation of HP-LT rocks and their tectonic implications in the western Tianshan Orogen, NW China: geochemical and age constraints. Lithos 66, 1-22.

Gao, J., Klemd, R., Zhang, L., Wang, Z., Xiao, X., 1999. P-T path of high-pressure/low-temperature rocks and tectonic implications in the western Tianshan Mountains, NW China. Jounal of

497 Metamorphic Geology 17, 621-636.
498 Grant, J.A., 2005. Isocon analysis: A brief review of the method and applications. Physics and Chemistry
499 of the Earth, Parts A/B/C 30(17–18), 997-1004.
500 Gresens, R.L., 1967. Composition-volume relationships of metasomatism. Chemical Geology 2, 47-65.
501 Guillong, M., Hametner, K., Reusser, E., Wilson, S.A., Gunther, D., 2005. Preliminary characterisation
502 of new glass reference materials (GSA-1G, GSC-1G, GSD-1G and GSE-1G) by laser
503 ablation-inductively coupled plasma-mass spectrometry using 193 nm, 213 nm and 266 nm
504 wavelengths. Geostandards and Geoanalytical Research 29(3), 315-331.
505 Haase, K.M., Freund, S., Koepke, J., Hauff, F., Erdmann, M., 2015. Melts of sediments in the mantle
506 wedge of the Oman ophiolite. Geology 43(4), 275-278.
507 Hermann, J., Rubatto, D., 2009. Accessory phase control on the trace element signature of sediment
508 melts in subduction zones. Chemical Geology 265(3-4), 512-526.
509 Hermann, J., Spandler, C., Hack, A., Korsakov, A.V., 2006. Aqueous fluids and hydrous melts in
510 high-pressure and ultra-high pressure rocks: Implications for element transfer in subduction
511 zones. Lithos 92, 399-417.
512 Hermann, J., Spandler, C.J., 2008. Sediment Melts at Sub-arc Depths: an Experimental Study. Journal of
513 Petrology 49(4), 717-740.
514 Herms, P., John, T., Bakker, R.J., Schenk, V., 2012. Evidence for channelized external fluid flow and
515 element transfer in subducting slabs (Raspas Complex, Ecuador). Chemical Geology 310–311,
516 79-96.
517 Hofmann, A.W., 1997. Mantle geochemistry: the message from oceanic volcanism. Nature 385(16),
518 219-229.
519 Jahn, B.M., Litvinovsky, B.A., Zanvilevich, A.N., Reichow, M., 2009. Peralkaline granitoid magmatism
520 in the Mongolian–Transbaikalian Belt: Evolution, petrogenesis and tectonic significance.
521 Lithos 113(3–4), 521-539.
522 John, T., Gussone, N., Podladchikov, Y.Y., Bebout, G.E., Dohmen, R., Halama, R., Klemd, R., Magna, T.,
523 Seitz, H.-M., 2012. Volcanic arcs fed by rapid pulsed fluid flow through subducting slabs.
524 Nature Geoscience 5, 489-492.
525 Jochum, K.P. et al., 2005. GeoReM: A New Geochemical Database for Reference Materials and Isotopic
526 Standards. Geostandards and Geoanalytical Research 29(3), 333-338.
527 John, T. et al., 2012. Volcanic arcs fed by rapid pulsed fluid flow through subducting slabs. Nature
528 Geoscience 5(7), 489-492.
529 John, T., Klemd, R., Gao, J., Garbe-Schonberg, C.D., 2008. Trace-element mobilization in slabs due to
530 non steady-state fluid-rock interaction: Constraints from an eclogite-facies transport vein in
531 blueschist (Tianshan, China). Lithos 103(1-2), 1-24.
532 Kelley, K.A., Plank, T., Farr, L., Ludden, J., Staudigel, H., 2005. Subduction cycling of U, Th, and Pb.
533 Earth and Planetary Science Letters 234(3-4), 369-383.
534 Kelley, K.A., Plank, T., Ludden, J., Staudigel, H., 2003. Composition of altered oceanic crust at ODP
535 Sites 801 and 1149. Geochemistry Geophysics Geosystems 4.
536 Keppler, H., 1996. Constraints from partitioning experiments on the composition of subduction-zone
537 fluids. Nature 380, 237-240.
538 Kerrick, D.M., Connolly, J.A.D., 2001. Metamorphic devolatilization of subducted marine sediments

and the transport of volatiles into the Earth's mantle. Nature 411, 293-296.
Klemd, R., Brocker, M., Hacker, B.R., Gao, J., Gans, P., Wemmer, K., 2005. New age constraints on the metamorphic evolution of the high-pressure/low-temperature belt in the western Tianshan Mountains, NW China. Journal of geology 113, 157-168.
Klemd, R., John, T., Scherer, E.E., Rondenay, S., Gao, J., 2011. Changes in dip of subducted slabs at depth: Petrological and geochronological evidence from HP–UHP rocks (Tianshan, NW-China). Earth and Planetary Science Letters 310(1–2), 9-20.
Lü, Z., Bucher, K., Zhang, L., 2013. Omphacite-bearing calcite marble and associated coesite-bearing pelitic schist from the meta-ophiolitic belt of Chinese western Tianshan. Journal of Asian Earth Sciences 76, 37-47.
Lü, Z., Zhang, L., 2012. Coesite in the eclogite and schist of the Atantayi Valley, southwestern Tianshan, China. Chinese Science Bulletin 57(13), 1467-1472.
Lü, Z., Zhang, L., Chen, Z., 2014. Jadeite- and dolomite-bearing coesite eclogite from western Tianshan, NW China. European Journal of Mineralogy 26(2), 245-256.
Lü, Z., Zhang, L.F., Du, J.X., Bucher, K., 2008. Coesite inlusions in garnet from eclogitic rocks in western Tianshan, northwest China: Convincing proof of UHP metamorphism. American Mineralogist 93, 1845-1850.
Lü, Z., Zhang, L.F., Du, J.X., Bucher, K., 2009. Petrology of coesite-bearing eclogite from Habutengsu Valley, western Tianshan, NW China and its tectonometamorphic implication. Journal of Metamorphic Geology 27, 773-787.
Li, J.-L., Klemd, R., Gao, J., Meyer, M., 2012. Coexisting carbonate-bearing eclogite and blueschist in SW Tianshan, China: Petrology and phase equilibria. Journal of Asian Earth Sciences 60, 174-187.
Li, J.-L., Gao, J., John, T., Klemd, R., Su, W., 2013. Fluid-mediated metal transport in subduction zones and its link to arc-related giant ore deposits: Constraints from a sulfide-bearing HP vein in lawsonite eclogite (Tianshan, China). Geochimica et Cosmochimica Acta 120, 326-362.
Li, J.-L., Klemd, R., Gao, J., John, T., 2016. Poly-cyclic Metamorphic Evolution of Eclogite: Evidence for Multistage Burial–Exhumation Cycling in a Subduction Channel. Journal of Petrology 57, 119-146.
Liu, Y.-H., Yang, H.-J., Takazawa, E., Satish-Kumar, M., You, C.-F., 2015. Decoupling of the Lu–Hf, Sm–Nd, and Rb–Sr isotope systems in eclogites and a garnetite from the Sulu ultra-high pressure metamorphic terrane: Causes and implications. Lithos 234–235, 1-14.
Liu, Y. et al., 2008. In situ analysis of major and trace elements of anhydrous minerals by LA-ICP-MS without applying an internal standard. Chemical Geology 257, 34-43.
Ludwig, K.R., 2003. User's manual for Isoplot 3.00: a geochronological toolkit for Microsoft Excel. Kenneth R. Ludwig.
Marschall, H.R., Schumacher, J.C., 2012. Arc magmas sourced from melange diapirs in subduction zones. Nature Geoscience 5(12), 862-867.
McCulloch, M.T., Gamble, J.A., 1991. Geochemical and geodynamicai constraints on subduction. Earth and Planetary Science Letters 102(3-4), 358-374.
Niu, Y.L., Batiza, R., 1997. Trace element evidence from seamounts for recycled oceanic crust in the Eastern Pacific mantle. Earth and Planetary Science Letters 148, 471-483.

581 Niu, Y.L., 2004. Bulk-rock major and trace element compositions of abyssal peridotites: Implications for
582 mantle melting, melt extraction and post-melting processes beneath mid-ocean ridges. Journal
583 of Petrology 45, 2423-2458.
584 Niu, Y., 2009. Some basic concepts and problems on the petrogenesis of intra-plate ocean island basalts.
585 Chinese Science Bulletin 54(22), 4148-4160.
586 Niu, Y., Gilmore, T., Mackie, S., Greig, A., Bach, W., 2002. Mineral chemistry, whole-rock compositions,
587 and petrogenesis of Leg 176 gabbros: data and discussion, Proceedings of the Ocean Drilling
588 Program, Scientific Results, pp. 1-60.
589 Niu, Y.L., O'Hara, M.J., 2003. Origin of ocean island basalts: A new perspective from petrology,
590 geochemistry, and mineral physics considerations. Journal of Geophysical Research 108(B4),
591 ECV5.1-ECV5.19.
592 Pearce, J.A., 2008. Geochemical fingerprinting of oceanic basalts with applications to ophiolite
593 classification and the search for Archean oceanic crust. Lithos 100, 14-48.
594 Rüpke, L.H., Morgan, J.P., Hort, M., Connolly, J.A.D., 2002. Are the regional variations in Central
595 American arc lavas due to differing basaltic versus peridotitic slab sources of fluids? Geology
596 30(11), 1035-1038.
597 Rüpke, L.H., Morgan, J.P., Hort, M., Connolly, J.A.D., 2004. Serpentine and the subduction zone water
598 cycle. Earth and Planetary Science Letters 223, 17-34.
599 Rubatto, D., Hermann, J., 2003. Zircon formation during fluid circulation in eclogites (Monviso, Western
600 Alps): Implications for Zr and Hf budget in subduction zones. Geochimica et Cosmochimica
601 Acta 67(12), 2173-2187.
602 Rubatto, D., Regis, D., Hermann, J., Boston, K., Engi, M., Beltrando, M., McAlpine, S.R.B., 2011.
603 Yo-yo subduction recorded by accessory minerals in the Italian Western Alps. Nature
604 Geoscience 4, 338-342.
605 Scambelluri, M., Pettke, T., Rampone, E., Godard, M., Reusser, E., 2014. Petrology and Trace Element
606 Budgets of High-pressure Peridotites Indicate Subduction Dehydration of Serpentinized Mantle
607 (Cima di Gagnone, Central Alps, Switzerland). Journal of Petrology 55(3), 459-498.
608 Schmidt, M.W., Vielzeuf, D., Auzanneau, E., 2004. Melting and dissolution of subducting crust at high
609 pressures: the key role of white mica. Earth and Planetary Science Letters 228, 65-84.
610 Shellnutt, J.G. et al., 2012. Origin of the silicic volcanic rocks of the Early Permian Panjal Traps,
611 Kashmir, India. Chemical Geology 334, 154-170.
612 Shen, T., Hermann, J., Zhang, L., Lü, Z., Padrón-Navarta, J.A., Xia, B., Bader, T., 2015. UHP
613 Metamorphism Documented in Ti-chondrodite- and Ti-clinohumite-bearing Serpentinized
614 Ultramafic Rocks from Chinese Southwestern Tianshan. Journal of Petrology 56, 1425-1458.
615 Sorensen, S.S., Grossman, J.N., Perfit, M.R., 1997. Phengite-hosted LILE enrichment in eclogite and
616 related rocks: Implications for fluid-mediated mass transfer in subduction zones and arc magma
617 genesis. Journal of Petrology 38, 3-34.
618 Spandler, C., Hermann, J., 2006. High-pressure veins in eclogite from New Caledonia and their
619 significance for fluid migration in subduction zones. Lithos 89, 135-153.
620 Spandler, C., Hermann, J., Arculus, R., Mavrogenes, J., 2003. Redistribution of trace elements during
621 prograde metamorphism from lawsonite blueschist to eclogite facies; implications for deep
622 subduction-zone processes. Contributions to Mineralogy and Petrology 146, 205-222.

623 Spandler, C., Hermann, J., Arculus, R., Mavrogenes, J., 2004. Geochemical heterogeneity and element
624 mobility in deeply subducted oceanic crust; insights from high-pressure mafic rocks from New
625 Caledonia. Chemical Geology 206, 21-42.
626 Spandler, C., Pettke, T., Hermann, J., 2014. Experimental study of trace element release during
627 ultrahigh-pressure serpentinite dehydration. Earth and Planetary Science Letters 391, 296-306.
628 Spandler, C., Pirard, C., 2013. Element recycling from subducting slabs to arc crust: A review. Lithos
629 170–171, 208-223.
630 Stern, R.J. et al., 2006. Subduction factory processes beneath the Guguan cross-chain, Mariana Arc: no
631 role for sediments, are serpentinites important? Contributions to Mineralogy and Petrology 151,
632 202-221.
633 Sun, S.-s., McDonough, W.F., 1989. Chemical and isotopic systematics of oceanic basalts: implications
634 for mantle composition and processes. Geological Society, London, Special Publications 42(1),
635 313-345.
636 Tatsumi, Y., 2005. The subduction factory: How it operates in evolving Earth. GSA Today 15(7), 4-10.
637 van der Straaten, F. et al., 2012. Tracing the effects of high-pressure metasomatic fluids and seawater
638 alteration in blueschist-facies overprinted eclogites: Implications for subduction channel
639 processes. Chemical Geology 292–293, 69-87.
640 van der Straaten, F., Schenk, V., John, T., Gao, J., 2008. Blueschist-facies rehydration of eclogites (Tian
641 Shan, NW-China): Implications for fluid-rock interaction in the subduction channel. Chemical
642 Geology 255, 195-219.
643 van Keken, P.E., Hacker, B.R., Syracuse, E.M., Abers, G.A., 2011. Subduction factory: 4. Depth
644 dependent flux of H_2O from subducting slabs worldwide. Journal of Geophysical Research
645 116, B01401.
646 Wei, C., Wang, W., Clarke, G.L., Zhang, L., Song, S., 2009. Metamorphism of High/ultrahigh-pressure
647 Pelitic–Felsic Schist in the South Tianshan Orogen, NW China: Phase Equilibria and P–T Path.
648 Journal of Petrology 50, 1973-1991.
649 Whitney, D.L., Evans, B.W., 2010. Abbreviations for names of rock-forming minerals. American
650 Mineralogist 95(1), 185-187.
651 Xiao, Y., Lavis, S., Niu, Y., Pearce, J.A., Li, H., Wang, H., Davidson, J., 2012. Trace-element transport
652 during subduction-zone ultrahigh-pressure metamorphism: Evidence from western Tianshan,
653 China. Geological Society of America Bulletin 124, 1113-1129.
654 Xiao, Y., Niu, Y., Li, H., Wang, H., Liu, X., Davidson, J., 2014. Trace element budgets and
655 (re-)distribution during subduction-zone ultrahigh pressure metamorphism: Evidence from
656 Western Tianshan, China. Chemical Geology 365, 54-68.
657 Xiao, Y., Niu, Y., Song, S., Davidson, J., Liu, X., 2013. Elemental responses to subduction-zone
658 metamorphism: Constraints from the North Qilian Mountain, NW China. Lithos 160–161,
659 55-67.
660 Xiao, Y., Niu, Y., Wang, K.-L., Lee, D.-C., Iizuka, Y., 2016. Geochemical behaviours of chemical
661 elements during subduction-zone metamorphism and geodynamic significance. International
662 Geology Review 58(10), 1253-1277.
663 Xiao, Y., Niu, Y., Zhang, H.-F., Wang, K.-L., Iizuka, Y., Lin, J., Tan, Y., Xu, Y., 2017. Effects of
664 decarbonation on elemental behaviors during subduction-zone metamorphism: Evidence from a

titanite-rich contact between eclogite-facies marble and omphacitite. Journal of Asian Earth Sciences 135, 338-346.

Yang, X., Zhang, L., Tian, Z., Bader, T., 2013. Petrology and U–Pb zircon dating of coesite-bearing metapelite from the Kebuerte Valley, western Tianshan, China. Journal of Asian Earth Sciences 70–71, 295-307.

Zack, T., John, T., 2007. An evaluation of reactive fluid flow and trace element mobility in subducting slabs. Chemical Geology 239, 199-216.

Zheng, Y.-F., Xia, Q.-X., Chen, R.-X., Gao, X.-Y., 2011. Partial melting, fluid supercriticality and element mobility in ultrahigh-pressure metamorphic rocks during continental collision. Earth-Science Reviews 107, 342–374.

Zheng, Y. F., 2012. Metamorphic chemical geodynamics in continental subduction zones.Chemical Geology 328, 5-48.

Zheng, Y.-F., and Hermann, J., 2014. Geochemistry of continental subduction-zone fluids. Earth Planets and Space 66, 93; doi:10.1186/1880-5981-66-93.

Zheng, Y.-F., Chen, Y.-X., 2016. Continental versus oceanic subduction zones. National Science Review 3, 495-519.

Zheng, Y. F., Chen, R. X., Xu, Z., Zhang, S.B., 2016. The transport of water in subduction zones. Science China: Earth Sciences 59, 651-682.

Supplementary Material

Supplementary data can be found in the online version of this article:

Table S.1 Major element contents of analyzed representative minerals by using EPMA.

Table S.2 Trace element contents of analyzed representative minerals with major elements for anhydrous minerals by using LA-ICP-MS.

Table S.3 Strontium and Nd isotope data of metamorphic rocks from the Chinese Western Tianshan HP-UHP metamorphic belt.

691 **Figure Captions**

692 **Figure 1** Geological sketch of the Chinese Western Tianshan HP-UHP metamorphic
693 terrane (after Lü et al., 2013; Li et al., 2013) and our sampling location for this study.

694 **Figure 2** Field photographs and photos for relationship of our rock samples. (a-b) show
695 the pillow-lava structure of our studied metabasaltic rock, i.e., omphacite-rich interiors
696 with glaucophane-rich rims, which represent the previous fluid flow passage. The white
697 dotted curve in (a) indicates the pillow margin, and the red dashed circle in (b) indicates
698 the drilling position for this study. Gln – glaucophane; Omp – omphacite. (c)
699 demonstrates the division of four sections from the top surface to the bottom of the
700 drilling core for this study. (d-g) are relevant slides for the four sections in (c). These
701 sections clearly show the decrease of glaucophane (bluish) and epidote (yellowish
702 green) modal abundances, but the increase of omphacite (green) abundance.

703 **Figure 3** Photomicrographs. (a) Relationship between omphacite-rich interiors and
704 glaucophane-rich rims. The mineral from omphacite-rich interiors can intervene
705 glaucophane-rich rims. (b) Glaucophane-rich rim, dominated by glaucophane and
706 epidote with phengite. (c-f) are for omphacite-rich interior, dominated by a matrix of
707 fine-grained omphacite and phengite with some glaucophane and epidote. (e) Locally
708 distributed coarse-grained apatite and omphacite. (f) Locally distributed carbonate,
709 which can be present as the inclusion of glaucophane porphyroblasts. Mineral
710 abbreviations used in this paper are: Aln – allanite; Ap – apatite; Ca – carbonate; Ep –

711 epidote; Gln – glaucophane; Omp – omphacite; Ph – phengite; Qz – quartz; Rt – rutile;
712 Ttn – titanite (mostly referred to Whitney and Evans, 2010).

713 **Figure 4** SEM-EDS photographs. See caption of Fig. 3 for mineral abbreviations. (a-c)
714 are for omphacite-rich cores, while (d-f) are for glaucophane-rich rims. (a) and (d)
715 display variable mineral inclusions in epidote porphyroblasts from the omphacite-rich
716 interior and glaucophane-rich rim respectively, including omphacite, phengite, rutile,
717 titanite and quartz. (b) A big glaucophane porphyroblast with its variable mineral
718 inclusions including titanite and rutile, and an epidote poikiloblast with omphacite,
719 rutile and phengite inclusions. (e) shows allanite composition core of the epidote
720 porphyroblast. (c,f) Abundant variable mineral inclusions in titanite with rutile
721 residuals, i.e., omphacite, phengite, and quartz. Epidote, glaucophane and titanite
722 poikiloblasts from both omphacite-rich interiors and glaucophane-rich rims generally
723 share similar mineral inclusions, i.e., omphacite, phengite, quartz, and rutile, which
724 indicate that these samples have experienced similar eclogite facies metamorphism.
725 Incl. – inclusion; porp. – porphroblast.

726 **Figure 5** Chondrite normalized mineral composition distributed diagrams (Sun and
727 McDonough, 1989). (a) Epidote from both the least and the most blueschist-facies
728 overprinted rocks with variably enriched Th-U-REEs-Pb-Sr; one allanite is highlighted.
729 (b) Phengite from both the least and the most blueschist-facies overprinted rocks
730 contains consistently high Ba-Rb-Cs contents. (c) Apatite with consistently high

731 REEs-Th-U-Sr. (d) Titnaite showing high Nb-Ta, some U and REEs. (e) Carbonate with
732 high Sr contents. (f) Glaucophane and omphacite contain insignificant trace element
733 contents.

734 **Figure 6** (a) Covariation diagram of Th/Yb and Nb/Yb for protolith fingerprint of our
735 subduction-zone metamorphosed rock samples (after Pearce, 2008). (b) E-MORB
736 normalized bulk-rock composition distributed diagram (Niu and O'Hara, 2003).
737 N-MORB and OIB are also plotted for comparison (Niu and O'Hara, 2003). The rocks
738 representing glaucophane-rich rims plot as blue circles, i.e., the bluest circles represent
739 rock 22A, while the light blue circles represent rock 22B. The rocks representing
740 omphacite-rich cores plot as yellowish circles, i.e., the light yellow circles represent
741 rock 22C, while the orange circles represent rock 22D. The legends used in Figs. 7-9
742 are also following these. The elements plotted in the grey areas (i.e., K-Ba-Rb-Pb-Sr)
743 are those mobilized by pervasive enrichment process covering the four rocks at the first
744 stage geochemical alteration in the subduction channel before the blueschist-facies
745 overprinting.

746 **Figure 7** (a) Rb-Sr isochron diagram of the four rock samples from the drilling core,
747 yielding a well-defined isochron age of 307±23 Ma (MSWD=6.9). (b) Initial Sr-Nd
748 isotopic compositions of the four rock samples from the drilling core are calculated
749 back to 310 Ma, and have been plotted in the mantle array. The legends used are the
750 same to Fig. 6. The initial Sr-Nd isotopes for metasomatic eclogites from the Chinese

751 Western Tianshan HP-UHP metamorphic belt in the study of van der Straaten et al.
752 (2012) are also plotted for comparison.

753 **Figure 8** Covariation diagrams for element contents and element ratio of bulk rocks
754 (after van der Straaten et al., 2012). (a) Ba/Rb – K. The relatively lower Ba/Ra of our
755 samples than seafloor basalts may reflect the effects of seafloor alteration before
756 subduction. (b) The correlated increase of Co and Ni contents with the increasing
757 degree of blueschist-facies overprint, indicating the large fluid fluxes are mainly
758 externally derived from serpentinite. The legends used are the same to Fig. 6.

759 **Figure 9** (a) Isocon diagram following the method of Grant (2005), taking 22D and
760 22A as the least and the most blueschist-facies overprinted rocks. Elements with the
761 individual slope within 1.000 ± 0.020, i.e., SiO_2, MnO, TiO_2, Ta, Zr and Hf (highlighted
762 in Table 1), are chosen as the reference elements to plot a best-fit linear array through
763 the origin as an isocon. The relevant equation and criterion for isochon plotting are
764 referred to Gresens (1967), Grant (2005) and van der Straaten et al. (2012). (b)
765 Bulk-rock trace element ratio changes with the blueschist-facies overprint. Th/Nb ratio
766 has been ten times for better clarification. The legends used are the same to Fig. 6.

767 **Figure 10** Co-variation diagrams for trace element contents of epidote from both the
768 least and the most blueschist-facies overprinted rocks (22D represented by the orange
769 solid circles vs. 22A represented by the blue solid circles). Allanite core of an epidote
770 porphyroblast has also been presented. The relationship of La with Pb (a) and Sr (b)

771 shows higher contents of Pb and Sr in epidote from 22A than of those from 22D,

772 resulting from the greatest addition of these elements by externally derived fluids.

773 **Table 1** Bulk-rock compositions of omphacite-rich interior and glaucophane-rich rim

774 of metabasaltic rock from the Chinese Western Tianshan HP-UHP metamorphic belt.

Figure 1 Geological map

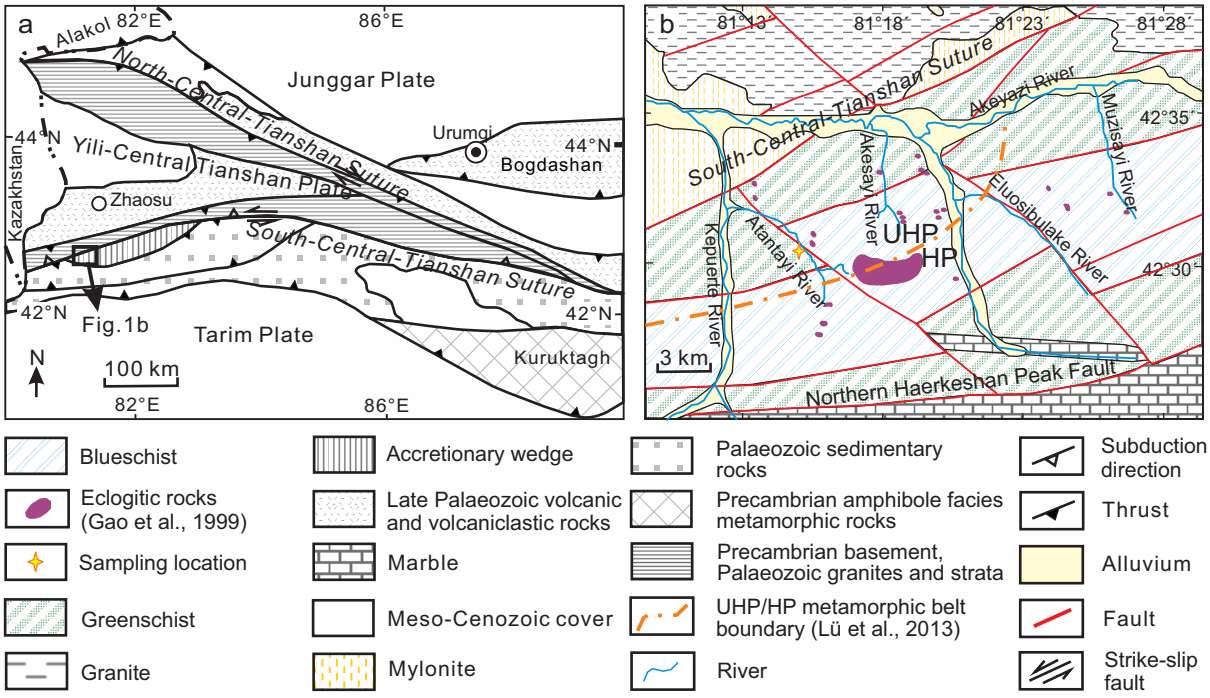

Figure 2 Rock photos

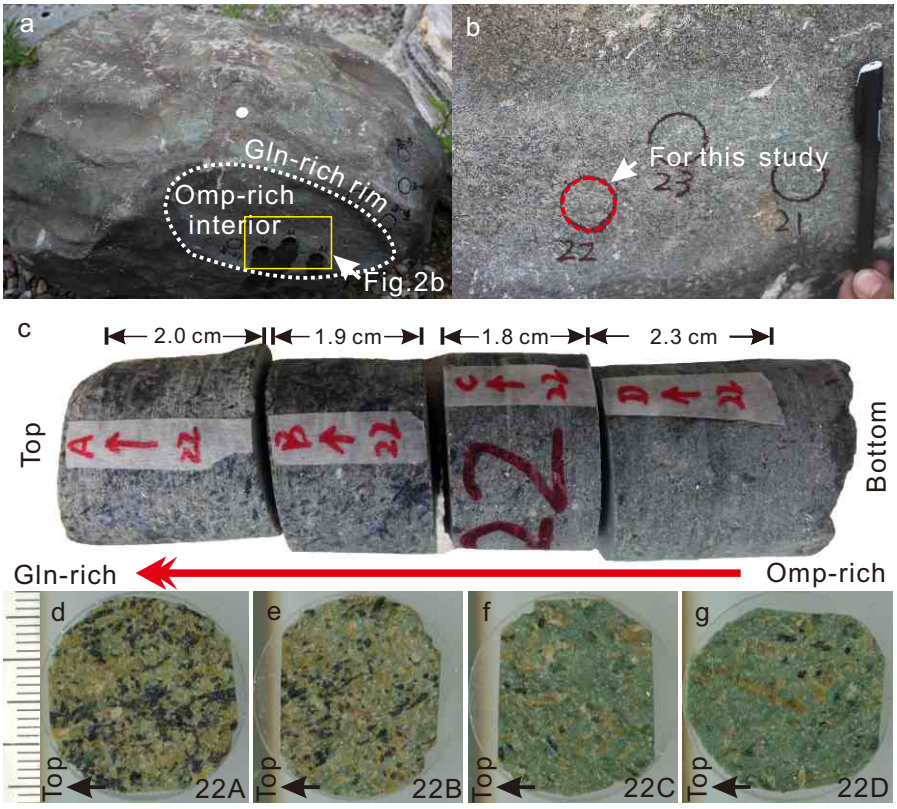

Figure 3 Photomicrographs

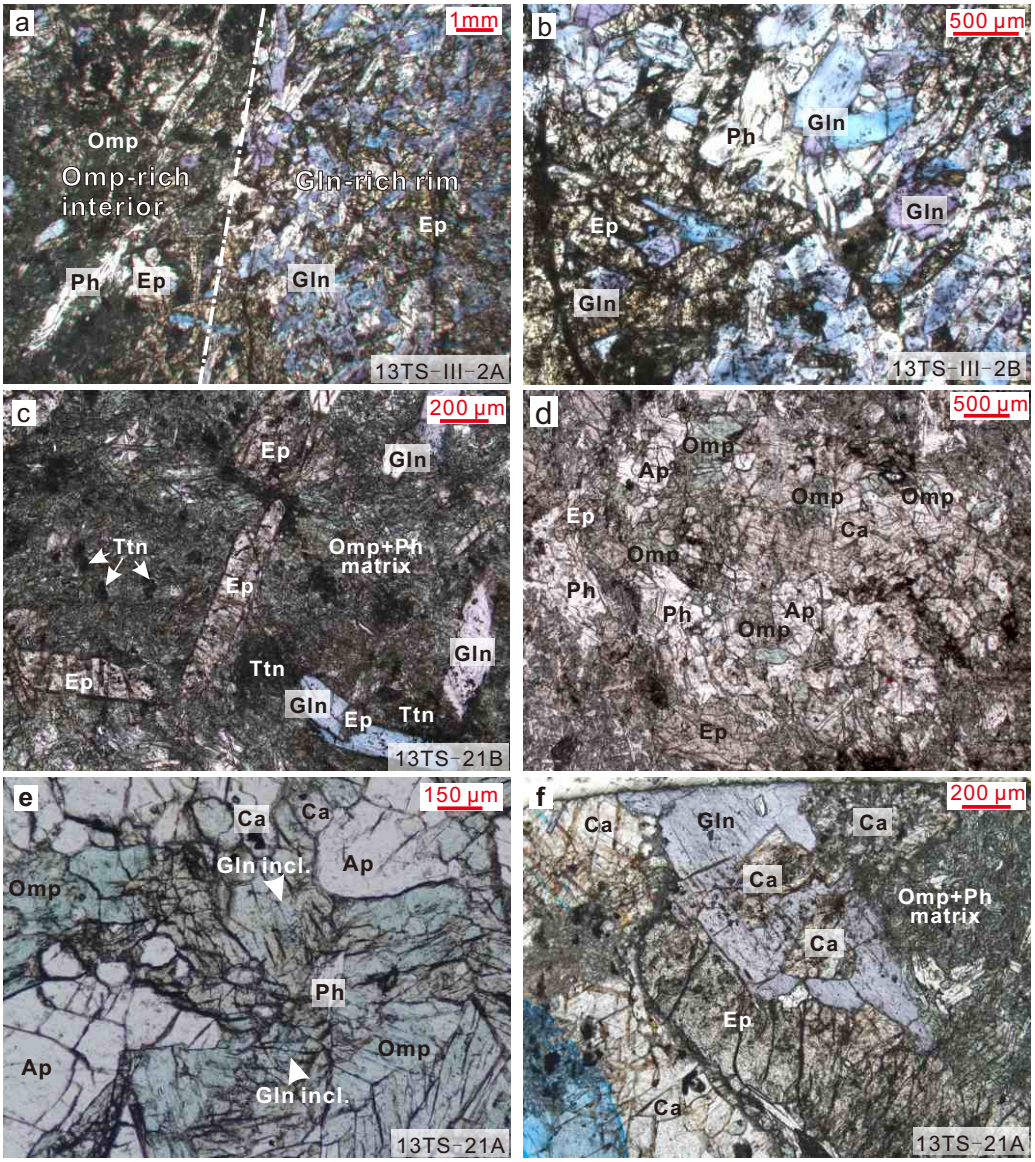

Figure 4 SEM-EDS photos

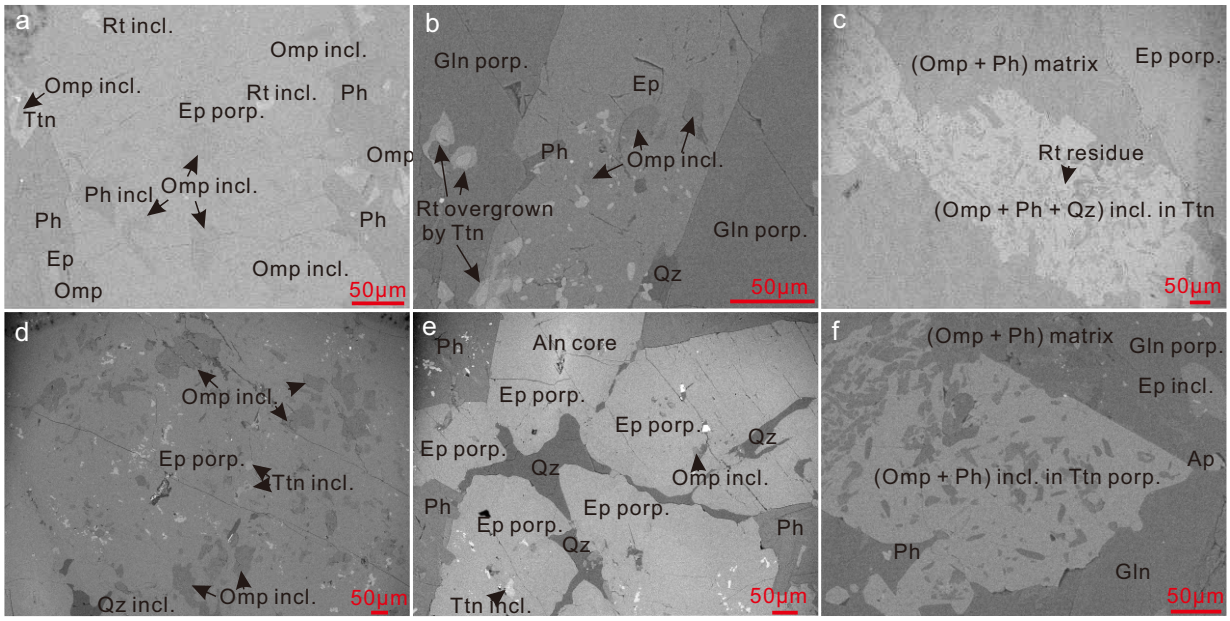

Figure 5 Mineral composition distribution

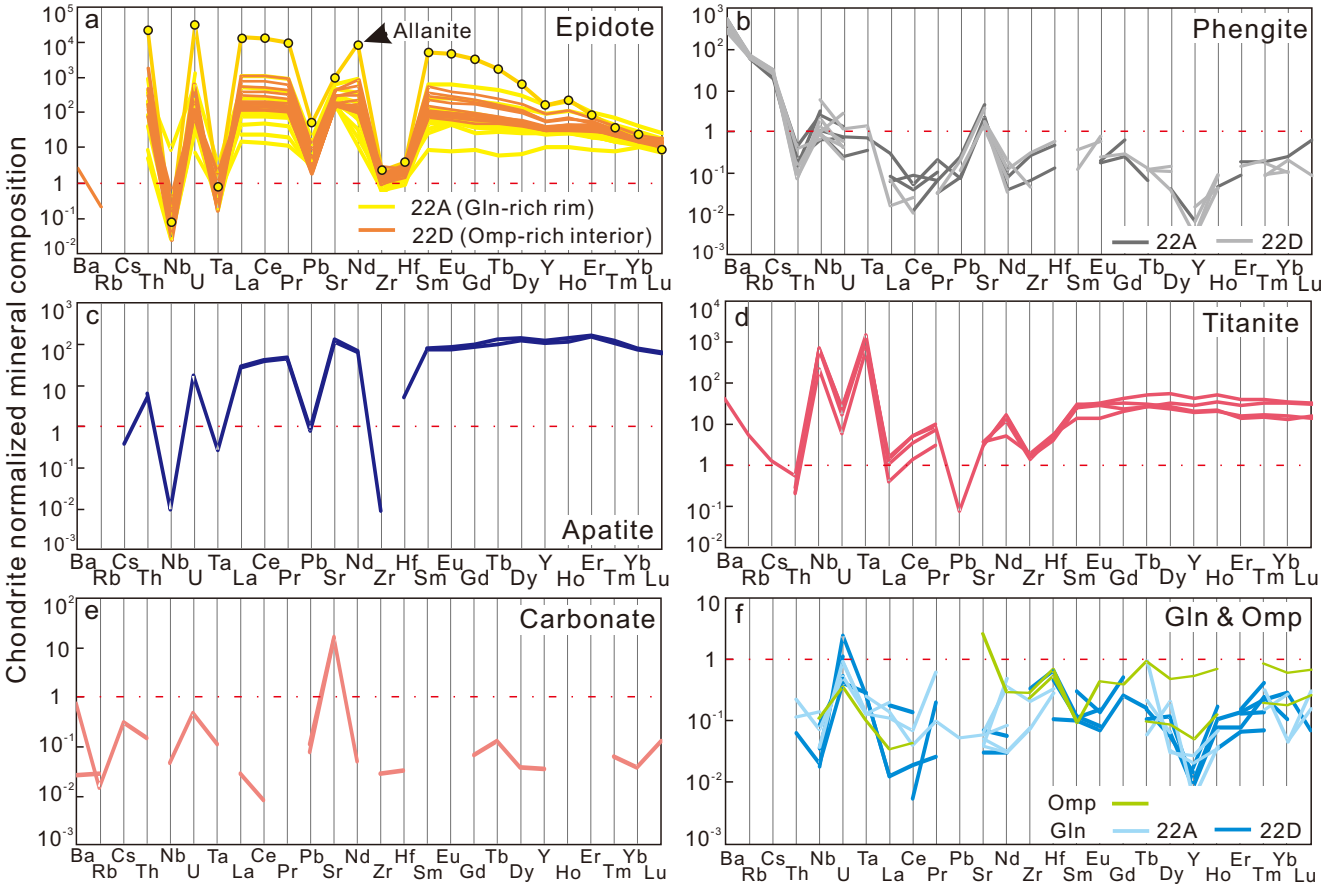

Figure 6 Fingerprint

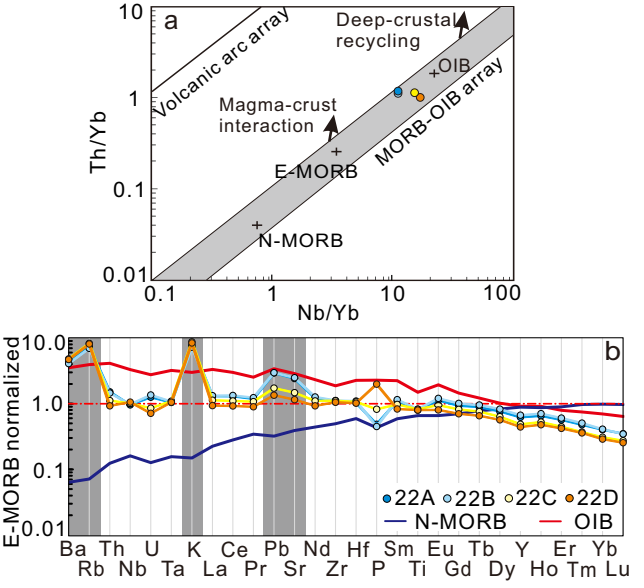

Figure 7 Sr-Nd isotope

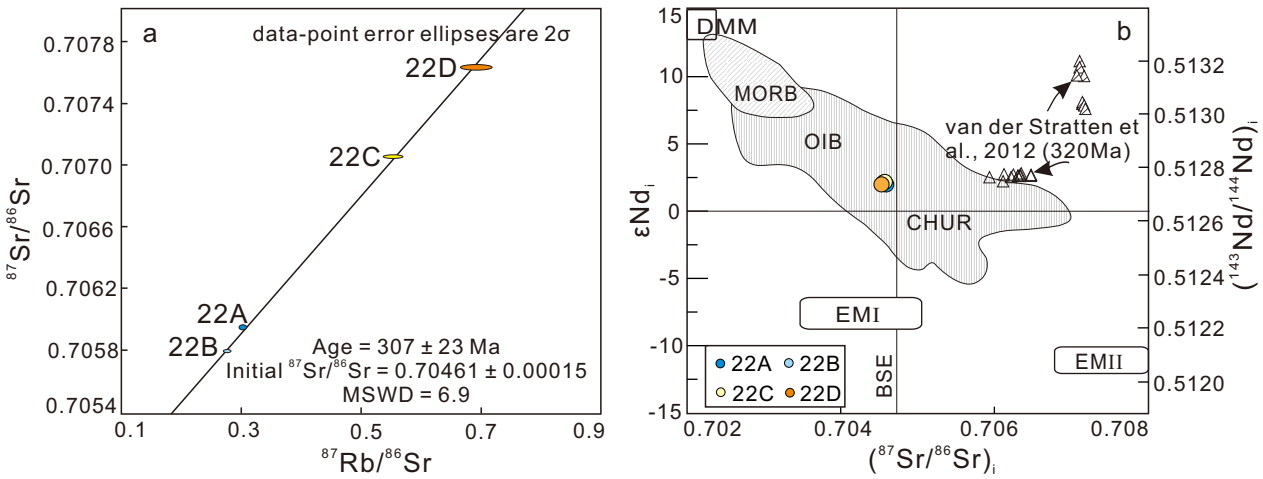

Figure 8 Seafloor alteration

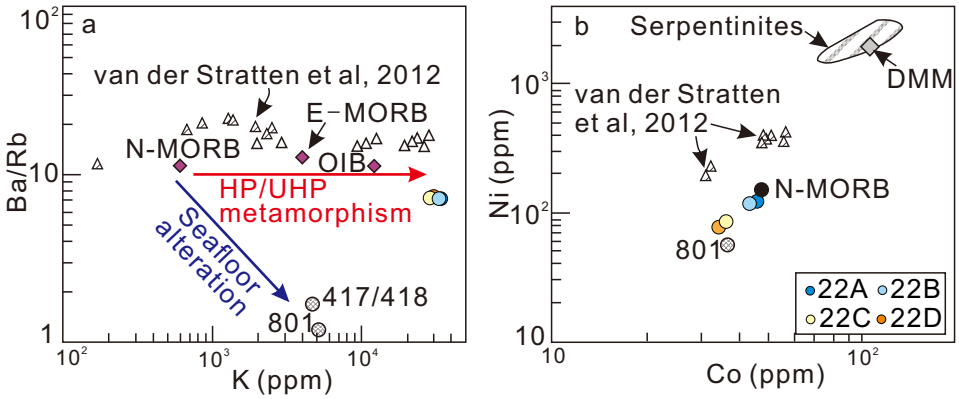

Figure 9 Mass balance

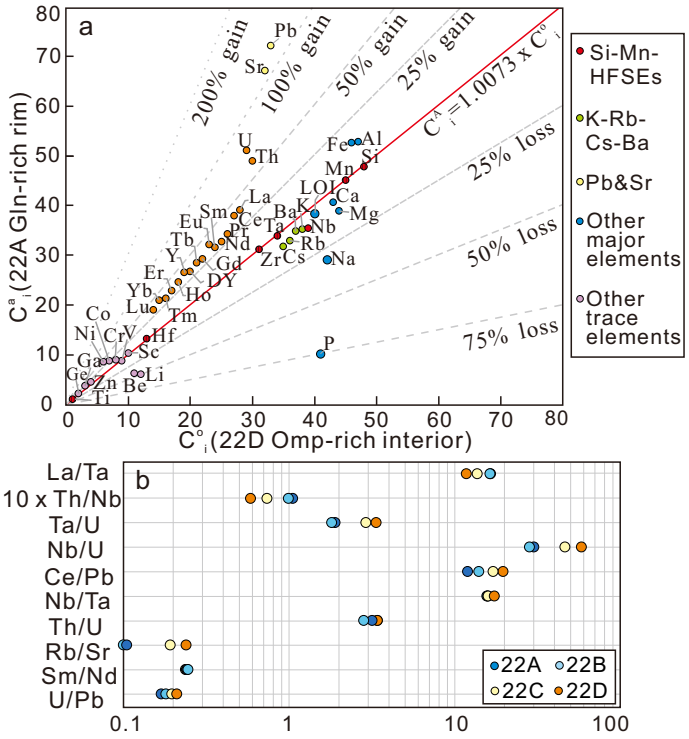

Figure 10 Mineral trace element co-variation

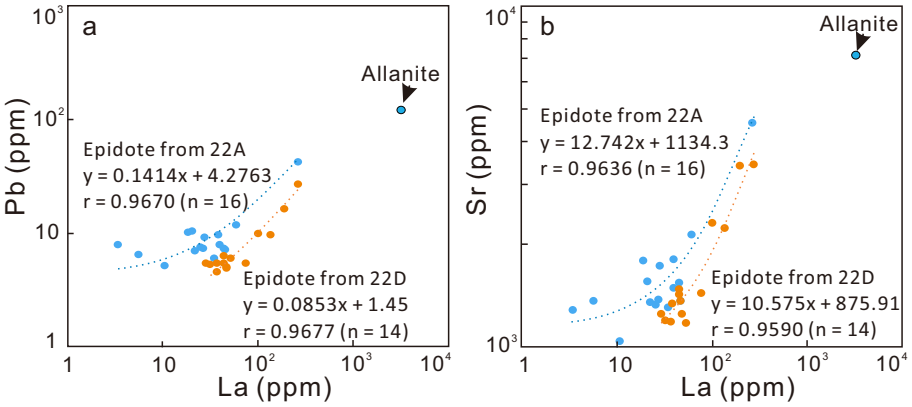

Graphical abstract

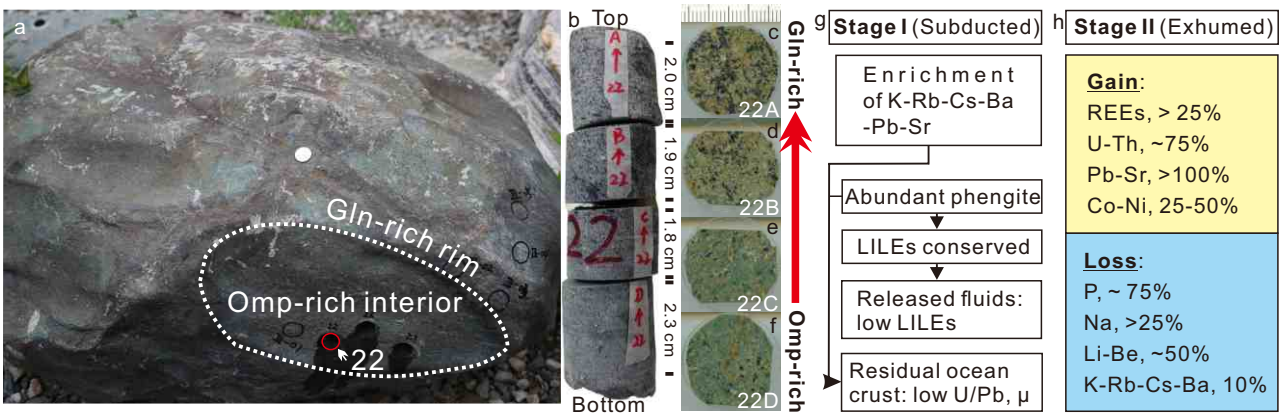

Table

Table 1 Bulk-rock compositions of omphacite-rich interior and glaucophane-rich rim of metabasaltic rock from the Chinese Western Tianshan HP-UHP metamorphic belt

	22A	**22B**	**22C**	**22D**	Slope to data point	Gain/Loss relative to 22D	Scaled	
Sample name	40% Gln + 15% Ph + 5% Omp + 40% Ep + some (Ttn + Ca)	20% Gln + 15% Ph + 20% Omp + 40% Ep + some (Ttn + Ca + Ap)	5% Gln + 25% Ph + 40% Omp + 25% Ep + 5% (Ttn + Ca + Ap)	5% Gln + 25% Ph + 50% Omp + 15% Ep + 5% (Ttn + Ca + Ap)	22A/22D	$\Delta C_i/C_i^o$	C_i^o (22D)	C_i^A (22A)
wt.%								
SiO_2	46.27	46.01	46.30	46.46	0.996	-0.011	48.00	47.80
TiO_2	1.51	1.56	1.56	1.52	0.993	-0.014	1.00	0.99
Al_2O_3	19.42	18.98	17.75	17.26	1.125	0.117	47.00	52.88
TFe_2O_3	7.68	7.76	6.59	6.71	1.145	0.136	46.00	52.65
MnO	0.04	0.04	0.04	0.04	1.000	-0.007	45.00	45.00
MgO	4.67	4.60	4.96	5.29	0.883	-0.124	44.00	38.84
CaO	9.78	10.49	10.49	10.35	0.945	-0.062	43.00	40.63
Na_2O	1.93	2.05	2.42	2.78	0.694	-0.311	42.00	29.16
K_2O	3.71	3.46	4.16	4.01	0.925	-0.082	38.00	35.16
P_2O_5	0.13	0.12	0.22	0.53	0.245	-0.756	41.00	10.06
LOI	4.42	4.51	5.05	4.61	0.959	-0.048	40.00	38.35
TOTAL	99.56	99.58	99.54	99.56				
ppm								
Li	8.09	8.67	13.4	15.9	0.510	-0.494	12.00	6.12
Be	0.87	0.93	1.40	1.53	0.571	-0.433	11.00	6.28
Sc	30.1	31.3	30.4	29.3	1.028	0.021	10.00	10.28
V	233	237	239	237	0.979	-0.028	9.00	8.81
Cr	177	177	175	159	1.114	0.106	8.00	8.91
Co	46.0	43.6	34.6	36.6	1.255	0.245	7.00	8.78
Ni	120	117	76.5	84.2	1.424	0.414	6.00	8.54
Cu	63.6	57.8	62.4	137	0.463	-0.541	5.00	2.31
Zn	74.9	71.2	60.1	65.4	1.144	0.136	4.00	4.58
Ga	24.2	24.1	20.2	18.9	1.281	0.272	3.00	3.84
Ge	1.27	1.34	1.18	1.13	1.122	0.113	2.00	2.24
Rb	57.4	53.8	64.0	62.6	0.916	-0.090	36.00	32.99
Sr	549	563	335	262	2.095	1.080	32.00	67.05
Y	19.4	20.9	15.2	13.8	1.401	0.390	19.00	26.61
Zr	156	165	164	155	1.008	0.001	31.00	31.26
Nb	13.8	14.0	14.5	15.1	0.908	-0.099	39.00	35.41
Cs	1.62	1.52	1.82	1.78	0.909	-0.098	35.00	31.81
Ba	434	400	470	461	0.941	-0.066	37.00	34.81
La	14.3	14.6	12.4	10.3	1.397	0.387	28.00	39.11
Ce	34.1	35.2	29.1	24.3	1.404	0.394	27.00	37.92
Pr	4.49	4.68	4.07	3.40	1.320	0.310	26.00	34.31
Nd	19.9	20.7	18.0	15.2	1.306	0.296	25.00	32.64
Sm	4.80	5.07	4.28	3.65	1.314	0.304	24.00	31.52
Eu	1.72	1.84	1.45	1.23	1.397	0.387	23.00	32.14
Gd	4.83	5.24	4.26	3.64	1.327	0.318	22.00	29.20
Tb	0.76	0.81	0.65	0.56	1.356	0.346	21.00	28.48
Dy	4.13	4.48	3.44	3.08	1.338	0.328	20.00	26.76
Ho	0.75	0.81	0.60	0.55	1.363	0.353	18.00	24.54
Er	1.86	1.97	1.46	1.38	1.347	0.337	17.00	22.90
Tm	0.22	0.23	0.17	0.17	1.331	0.321	16.00	21.29
Yb	1.23	1.26	0.95	0.89	1.392	0.382	15.00	20.88
Lu	0.16	0.16	0.13	0.12	1.365	0.355	14.00	19.11
Hf	3.52	3.74	3.64	3.47	1.015	0.007	13.00	13.19
Ta	0.87	0.90	0.91	0.88	0.995	-0.012	34.00	33.82
Pb	2.72	2.74	1.60	1.24	2.185	1.169	33.00	72.10
Th	1.45	1.39	1.07	0.89	1.633	0.621	30.00	48.98
U	0.46	0.50	0.31	0.26	1.758	0.746	29.00	51.00
La/Ta	16.5	16.3	13.7	11.7				
Th/Nb	0.11	0.10	0.07	0.06				
Ta/U	1.90	1.81	2.90	3.35				
Nb/U	30.0	28.2	46.2	58.0				
Ce/Pb	12.6	12.8	18.2	19.5				
Nb/Ta	15.8	15.6	15.9	17.3				

Table S.1 Major elements of hydrous minerals

Click here to download Supplementary Interactive Plot Data (CSV): XiaoEtAl-JAES-Table S.1 Mineral major elements_XIAO.x

Table S.2 LA-ICP-MS data for mineral trace elements

Click here to download Supplementary Interactive Plot Data (CSV): XiaoEtAl-JAES-Table S.2 Mineral trace elements_XIAO.xl

Table S.3 Isotopic composition

Click here to download Supplementary Interactive Plot Data (CSV): XiaoEtAl-JAES-Table S.3 Isotopic composition.xlsx